



Morphology and oxidation state of ALD-grown Pd nanoparticles on TiO₂- and SrO-terminated SrTiO₃ nanocuboids



Bor-Rong Chen^a, Cassandra George^b, Yuyuan Lin^a, Linhua Hu^b, Lawrence Crosby^a, Xianyi Hu^a, Peter C. Stair^b, Laurence D. Marks^a, Kenneth R. Poeppelmeier^b, Richard P. Van Duyne^b, Michael J. Bedzyk^a

^a Department of Materials Science and Engineering, Northwestern University, Evanston, IL 60208, USA

^b Department of Chemistry, Northwestern University, Evanston, IL 60208, USA

ARTICLE INFO

Available online 7 November 2015

Keywords:

Supported palladium nanoparticles
Strontium titanate
Atomic layer deposition
X-ray absorption spectroscopy
Electron microscopy
X-ray photoemission spectroscopy

ABSTRACT

We employ SrTiO₃ nanocuboid single crystals with well-defined (001) surfaces that are synthesized to have either a TiO₂- or SrO-terminated surface to investigate the influence of surface termination on the morphology and the chemical property of supported metallic nanoparticles. Using such monodispersed STO nanocuboids allows for practical catalytic reaction studies as well as surface studies comparable to a single crystal model catalyst. Pd nanoparticles were grown by atomic layer deposition, which is able to control the effective coverage, chemical state, and the size of the Pd nanoparticles. The properties of Pd nanoparticles were examined by transmission electron microscopy, X-ray absorption spectroscopy, and X-ray photoemission spectroscopy. The morphology and growth pattern for the Pd nanoparticles supported on the SrTiO₃ nanocuboids are shown to depend on the surface termination.

© 2015 Elsevier B.V. All rights reserved.

1. Introduction

It is well known that the support oxide in heterogeneous catalysts has a pronounced influence on the physical and chemical properties of supported metal nanoparticles. The support oxide may participate in the reaction directly, introduce charge transfer from/to the nanoparticles, or alter the shape and size of the supported metal nanoparticles. The thermodynamic equilibrium shape of supported metal nanoparticles can be determined by the Winterbottom construction [1], which links the relative surface and interface energies between nanoparticle/support oxide to the equilibrium shape of nanoparticle. The Winterbottom construction governs the degree of truncation of metal nanoparticle by the support, and gives insight into nanoparticle engineering of catalysts with precise control of the morphology.

In order to study the structure–activity relationship, there is a “materials gap” that needs to be filled. Traditional model catalysts used in surface science studies are usually single-crystals, for which the surface–area-to-volume ratio is too small for practical catalytic reactions. Alternatively, the surfaces of support oxides used commercially are usually poorly defined, making it difficult to correlate the measured catalytic effects to the atomic-scale interface and nanoparticle structure. Our approach to minimize the “materials gap” is using a controlled nanoscale support material with well-defined surfaces. SrTiO₃ (STO) nanoparticles can be synthesized with distinct faceting [2–5]. Our approach follows previously established work [6–9] utilizing SrTiO₃ nanocuboids with low size dispersion and well-defined (001) surfaces as the support material of the catalytic nanoparticles. In this study, TiO₂- and SrO-terminated surfaces of STO nanocuboids [10] are utilized

to study the effect of surface termination on the morphology and chemical state of the supported nanoparticles in a way that excludes the intrinsic chemical difference when comparing nanoparticles on support oxides with different bulk compositions.

Pd and Pt are active catalytic metals and both have a lattice constant close to that of STO ($a_{\text{Pd}} = 3.89 \text{ \AA}$, $a_{\text{Pt}} = 3.92 \text{ \AA}$, $a_{\text{STO}} = 3.905 \text{ \AA}$). Earlier studies of Pt and Pd nanoparticles supported on single crystal STO substrates as model systems for investigating properties of the nanoparticles such as morphology [11–18], photolysis performance [19], and interfacial atomic correlations with the STO lattice [11,20–22]. Moving from single crystal to faceted nanoparticle supports, it has been demonstrated recently that Pt/STO nanocuboid catalyst systems have high thermodynamic and sintering resistance due to the strong cube-on-cube epitaxy at the interface [8]. Furthermore, when SrTiO₃ nanocuboids are substituted with Ba_{0.5}Sr_{0.5}TiO₃ nanocuboids, the Winterbottom truncation of Pt nanoparticles leads to the corresponding change predicted by lattice mismatch and interfacial free energy. As shown earlier, the shape of the Pt nanoparticle can be controlled by the support in a predictable manner [8]. Pd, with similar lattice constants and chemical properties as those of Pt, is expected to show similar behavior.

In this study, Pd deposition was carried out by atomic layer deposition (ALD). It has been recognized that ALD is capable of synthesizing supported transition metal nanoparticles, such as Pd, Pt and Ru on various supports [6,16–18,23–26]. ALD also has the ability to fine tune the amount of metal deposited by the number of ALD cycles. However, the growth of ALD-synthesized metal nanoparticles at the early stage is still poorly understood, especially for the deposition of Pd. Pd/STO samples

with different numbers of ALD cycles have been prepared in the current study and characterized by transmission electron microscopy (TEM) and X-ray absorption spectroscopy (XAS) to reveal and compare their morphology, chemical state, and local atomic coordination structure.

2. Materials and methods

2.1. Sample preparation

Single crystal SrTiO₃ (STO) nanocuboids with well-defined (001) faces were synthesized to have predominantly SrO- or TiO₂-terminated surfaces by acetic acid- [2,3] and oleic acid-assisted methods [4] respectively. The nanocuboids are in the form of a dry, white powder. High resolution transmission electron microscopy (HRTEM) experiments and density function theory (DFT) simulation were previously used to determine the surface termination of the STO nanocuboids [10]. The SrO-terminated STO nanocuboids, synthesized by the steps described in [4], were washed with ethanol then calcined in air at 450 °C for 3 h in order to remove the residual oleic acid ligands. Standard Brunauer–Emmett–Teller (BET) analysis determined that the surface area was 20 m²/g for the TiO₂-terminated nanocuboids, and 61 m²/g for the SrO-terminated nanocuboids. The mean edge length for the TiO₂-terminated nanocuboids is 67 nm with a standard deviation (SD) of 12.5 nm; for the SrO-terminated nanocuboids, the mean is 15 nm with 2.8 nm SD. See Fig. S1 in the Supplementary material (SM) for the size distribution histograms and BET analysis.

The Pd ALD process was conducted in a viscous-flow ALD reactor [27]. Before ALD growth, both TiO₂-STO and pre-treated SrO-STO nanocuboids were heated in the ALD reactor at 200 °C for 10 min in nitrogen gas to equilibrate the temperature of the STO nanoparticles. This was followed by ozone treatment at 200 °C for 30 min to remove surface carbon. Pd(II) hexafluoroacetylacetonate (Pd(hfac)₂) and formalin (HCHO) were used as the precursors in the ALD process [23]. The reactant exposures lasted 300 s for each precursor, and nitrogen purges of 300 s were performed in between each precursor exposure and after the last exposure. After ALD processing, the samples were removed from the reactor and cooled in air. Samples were prepared with 1, 5, 10, and 20 cycles (denoted as 1c, 5c, 10c and 20c) of Pd ALD grown on the TiO₂-terminated STO nanocuboids, and with 1c, 5c, and 10c of Pd on the SrO-terminated nanocuboids. The Pd/STO samples were in the form of a dry powder, with a gray-scale color gradient that was darker for increased cycles of Pd.

2.2. Characterizations

2.2.1. Morphology and loading of Pd

The morphology of the as-deposited Pd/STO samples was examined by a JEOL 2100F TEM. The sizes and shapes of a large representative group of Pd nanoparticles for the 5c and 10c samples were measured using the ImageJ software [28].

The atomic percentage ratio between Pd and Sr of the Pd/STO samples was measured by both inductively coupled plasma atomic emission spectroscopy (ICP-AES) and X-ray fluorescence (XRF). The ratio was

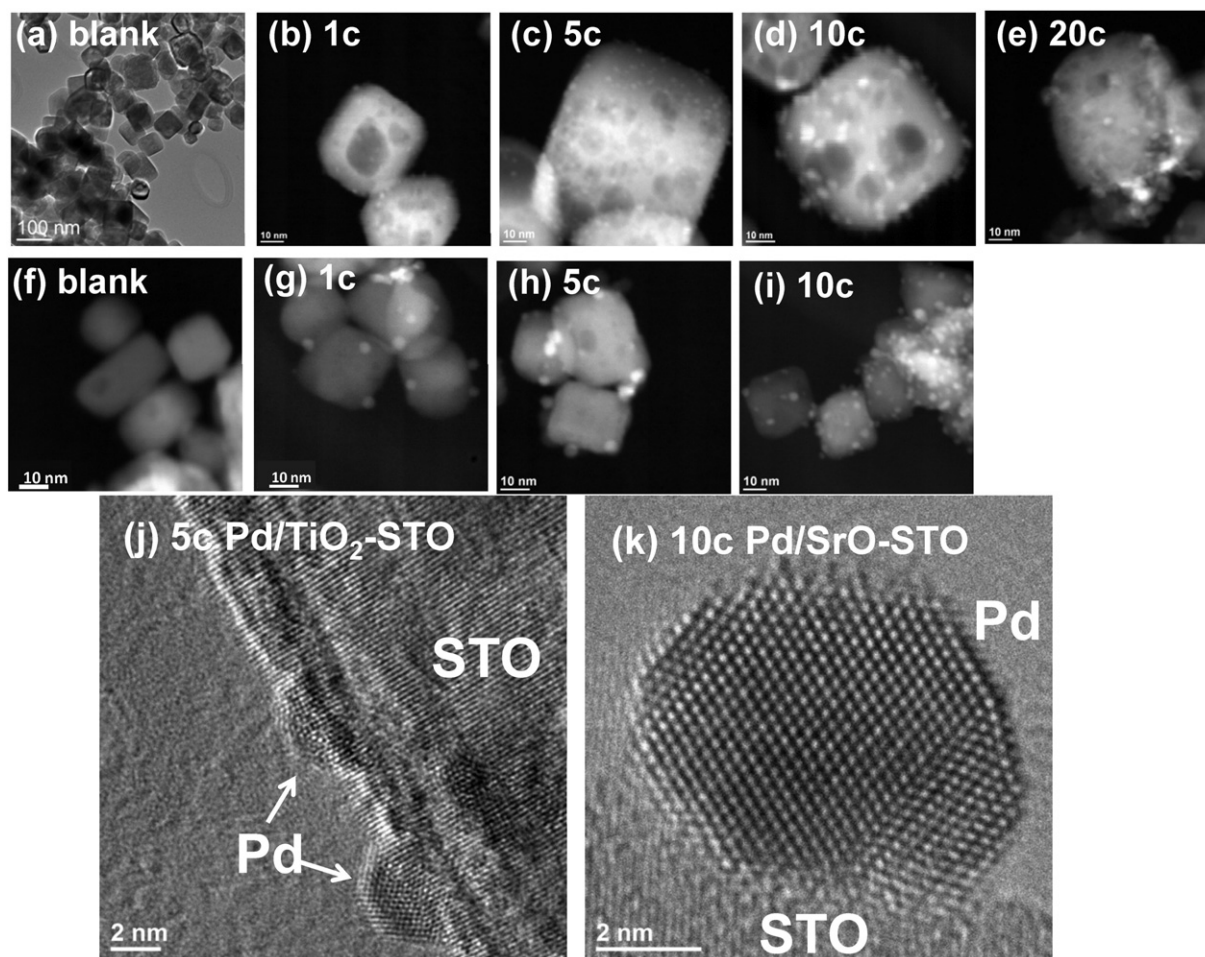


Fig. 1. TEM and HAADF images of TiO₂-terminated (a–e) and SrO-terminated SrTiO₃ (f–i) nanocuboids before and after ALD Pd deposition. Pd nanoparticles can be clearly seen from the images. HRTEM images in (j) and (k) show the details of the faceted Pd nanoparticles on TiO₂-terminated and SrO-terminated STO surfaces. A better wetting between Pd and the TiO₂-STO surface can be observed.

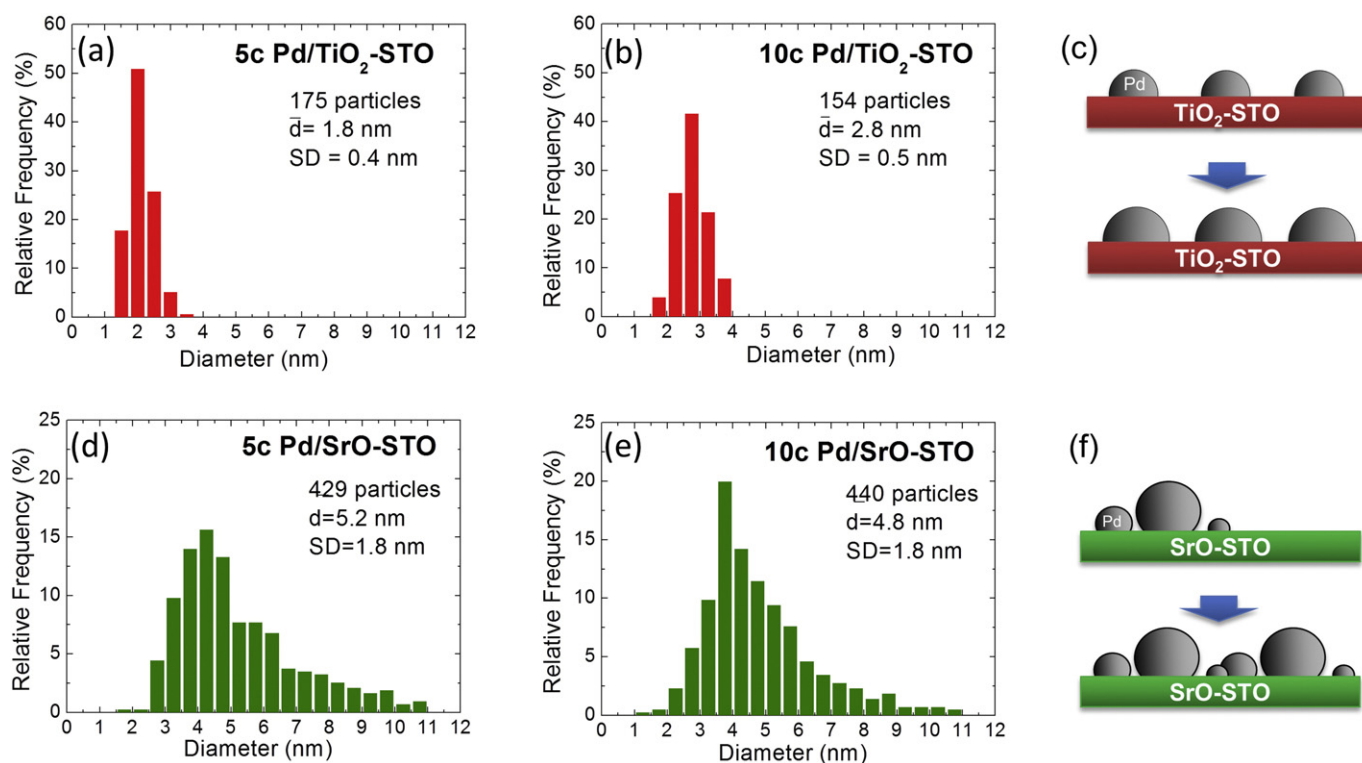


Fig. 2. Histograms of Pd nanoparticle diameters extracted from TEM images: size distribution of 5c Pd/TiO₂-STO (a), 10c Pd/TiO₂-STO (b), 5c Pd/SrO-STO (d), and 10c Pd/SrO-STO (e). The mean diameter (\bar{d}) and standard deviation (SD) values are included in the figure. Schematic representations of the morphology and evolution of Pd nanoparticles on TiO₂- and SrO-terminated STO surface are shown in (c) and (f), respectively.

then converted into Pd wt% loading and coverage. For ICP-AES, the Pd/STO sample was dissolved in aqua regia for 24 h and then analyzed by a Varian Vista MPX ICP Spectrometer. XRF measurements were performed at beamline 5BM-D at the Advanced Photon Source (APS) at Argonne National Laboratory at an incident photon energy of 24.4 keV. (See SM for analysis details.)

2.2.2. XANES and EXAFS

All the X-ray absorption near edge structure (XANES) and extended X-ray absorption fine structure (EXAFS) measurements were completed at beamline 5BM-D at the APS. The Pd atom oxidation state(s) and its local atomic coordination structure were analyzed by XANES and EXAFS, respectively. These ex-situ (open air) XANES and EXAFS measurements of the as-deposited samples were carried out around the Pd K edge (24.4 keV) in fluorescence with the sample under ambient atmosphere. Data processing was completed with the ATHENA and ARTEMIS software packages [29]. The coordination numbers (N)

of Pd-Pd and Pd-O bonds, Pd-Pd and Pd-O bond distances (R), and Debye-Waller factors (σ), were obtained by a least-squares fitting in R -space between 1–3.5 Å of the k^2 -weighted Fourier transformed EXAFS data ($k = 2.5\text{--}11 \text{ \AA}^{-1}$). Photoelectron scattering paths used in the fitting were based on the first nearest neighbors of Pd in FCC Pd (Pd-Pd) and tetragonal PdO (Pd-O) (see Fig. S3 for details).

In addition to the above described ex-situ X-ray spectroscopy measurements, an X-ray flow cell [30] was employed for in-situ XANES and EXAFS experiments on a select set of samples. The Pd/STO sample was pre-reduced under flowing H₂ at 300 °C for 30 min to remove the Pd surface oxide, and the measurements were completed in an H₂ flow at room temperature during the in-situ measurements. Additionally, to investigate the change of the Pd oxidation state under

Table 1

The atomic percentage ratio of Pd and Sr can be directly measured from both ICP-AES (inductively coupled plasma atomic emission spectroscopy) and XRF (X-ray fluorescence). Pd loading and the effective Pd coverage (θ) can then be calculated by assuming that the atomic ratio of Sr:Ti:O in the SrTiO₃ nanocuboids is exactly 1:1:3.

Termination	Cycles	Pd/Sr (at.% ratio)		Pd loading (wt.%)		Effective Pd coverage, θ (ML)	
		ICP	XRF	ICP	XRF	ICP	XRF
TiO ₂	1c	0.015	0.012	0.86	0.73	0.34	0.29
	5c	0.037	0.031	2.1	1.7	0.84	0.7
	10c	0.052	0.070	2.9	3.9	1.2	1.6
	20c	0.13	0.15	6.8	8.1	2.9	3.4
SrO	1c	0.014	0.016	0.86	0.94	0.12	0.14
	5c	0.063	0.064	3.5	3.6	0.52	0.53
	10c	0.11	0.11	5.8	5.9	0.86	0.88

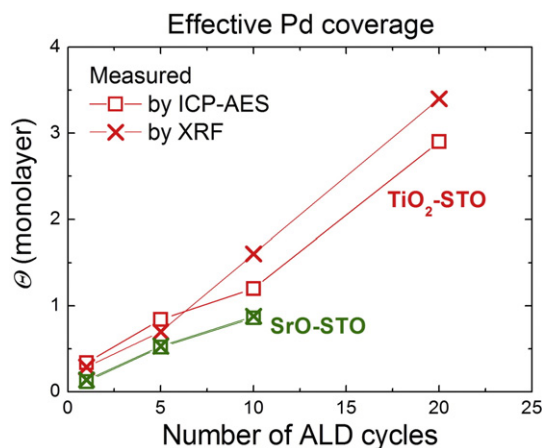


Fig. 3. Effective Pd coverage (θ) increases almost linearly as the number of ALD cycles increases. One monolayer ($\theta = 1 \text{ ML}$) coverage is defined as the 2D density of Sr atom in a SrO (001) atomic plane of STO (6.56 nm^{-2}).

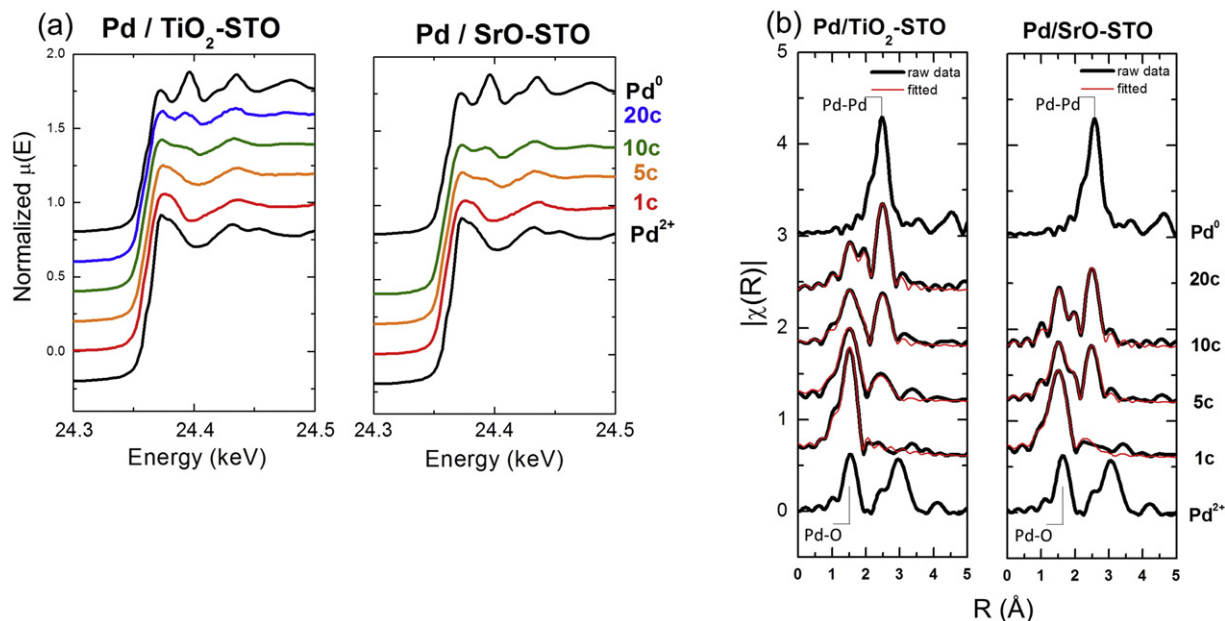


Fig. 4. (a) The Pd K edge X-ray absorption spectra for the ALD-Pd/STO samples with different numbers of ALD cycles. The Pd K-edge of a Pd foil (Pd^0) and PdO (Pd^{2+}) powder references are shown for comparison. (b) Fourier transform magnitudes of k^2 -weighted Pd K-edge EXAFS spectra, along with the corresponding first shell fit (red lines). Pd-O and Pd-Pd first shell coordination numbers can be extracted from the best fit of the EXAFS data.

redox environments similar to a real catalytic reaction, in-situ XANES measurements were carried out by exposing the samples to redox atmospheres. The sample was heated to 300 °C in the X-ray flow cell under pure O_2 and held at that temperature for 30 min, and then the cell was purged with N_2 at a rate of 10 mL/min for 30 min and cooled to room temperature. The XANES measurements were completed in an N_2 flow at room temperature. The reaction gas was then switched to 3% H_2/N_2 , and the procedure described above was applied to the H_2 cycle. The N_2 purge step after the H_2 exposure removed the excess H_2 in the cell, thus prevented Pd hydride formation.

2.2.3. X-ray photoemission analysis

The surface species on the Pd/STO samples were analyzed with X-ray photoemission spectroscopy (XPS, Thermo Scientific ESCALAB 250Xi) using a monochromatic Al $K\alpha$ (1486.74 eV) X-ray source. The atomic ratio between surface F and surface Sr atoms was obtained by analyzing the peak area covered by F 1s and Sr 3d core level photoemission peaks (see SM for details).

3. Results and discussion

3.1. Morphology analysis

Fig. 1 presents TEM and high angle annular dark field (HAADF) images of the Pd/SrTiO₃ samples, which shows the Pd formed nanoparticles on the surface of the STO nanocuboids. The images of the 5c and 10c samples are representative and establish the morphology and growth trends of Pd nanoparticles on TiO₂- and SrO-terminated surfaces of STO. The sizes and shapes of a large representative group of Pd nanoparticles for the 5c and 10c samples were measured using the ImageJ software [28]. The histograms for the nanoparticle diameters are shown in Fig. 2 along with the statistical analysis determining the mean values for the diameters (\bar{d}) and the standard deviations (SD). The shape of the Pd nanoparticle is described by an “aspect ratio,” which is defined as the maximum height of the Pd nanoparticle perpendicular to the surface divided by the maximum width parallel to the surface. On the TiO₂-terminated STO surface, the shape of Pd nanoparticles is flatter, with a mean aspect ratio of $\sim 0.6(1)$, while Pd nanoparticles

Table 2
Fitting parameters of Pd K edge EXAFS of as-deposited Pd/SrTiO₃ nanocuboids, including the first nearest neighbor coordination numbers (N), bond distances (R), EXAFS Debye–Waller factors (σ), and energy shifts (ΔE) for Pd–Pd and Pd–O scattering paths.

		$N_{\text{Pd-Pd}}$	$R_{\text{Pd-Pd}}$ (Å)	$\sigma_{\text{Pd-Pd}}$ (Å)	$\Delta E_{\text{Pd-Pd}}$ (eV)*	$N_{\text{Pd-O}}$	$R_{\text{Pd-O}}$ (Å)	$\sigma_{\text{Pd-O}}$ (Å)	$\Delta E_{\text{Pd-O}}$ (eV)*
Pd foil		12	2.75	0.074**	0				
PdO (II)						4	2.01		0
Termination	# cycles								
TiO ₂	1c	1.0 ± 1.0	2.69 ± 0.10	0.11 ± 0.02	5.1 ± 3.5	3.2 ± 0.4	2.01 ± 0.01	0.04 ± 0.01	2.1 ± 1.5
	5c	2.4 ± 1.5	2.72 ± 0.05	0.11 ± 0.02	0.2 ± 4.7	3.0 ± 0.6	2.01 ± 0.02	0.05 ± 0.02	2.0 ± 2.6
	10c	3.4 ± 1.1	2.70 ± 0.02	0.10 ± 0.02	−3.1 ± 2.6	1.7 ± 0.5	2.01 ± 0.02	0.05 ± 0.02	1.5 ± 3.8
	20c	4.8 ± 0.3	2.72 ± 0.02	0.09 ± 0.02	−3.6 ± 2.8	1.1 ± 0.8	2.01 ± 0.07	0.06 ± 0.01	3.7 ± 1.8
SrO	1c	1.2 ± 0.9	2.71 ± 0.06	0.10 ± 0.05	2.7 ± 2.6	3.2 ± 0.6	2.01 ± 0.01	0.06 ± 0.02	3.5 ± 1.7
	5c	3.0 ± 1.1	2.71 ± 0.03	0.09 ± 0.02	0.1 ± 3.1	1.8 ± 0.6	2.01 ± 0.03	0.06 ± 0.02	3.5 ± 4.1
	10c	4.2 ± 0.8	2.72 ± 0.02	0.10 ± 0.01	−3.1 ± 1.8	1.3 ± 0.4	2.01 ± 0.02	0.05 ± 0.02	1.5 ± 3.9

* The value of ΔE can either be a positive or negative number. Therefore, a fitted ΔE value like 2.0 ± 2.6 will be acceptable. The acceptable range of ΔE is in between -10 and 10 eV.

** The value of $\sigma_{\text{Pd-Pd}}$ of Pd foil (0.074 Å) was calculated from the Debye temperature of Pd, $\theta_{\text{D, Pd}} = 274$ K.

on the SrO-terminated surface have a higher aspect ratio $\sim 0.8(1)$. The difference in the wetting behavior provides some insight into the interfacial energy between Pd and the STO nanocuboids based on Winterbottom construction [1]. The smaller aspect ratios (see SM for statistical details), or better wetting, between Pd and the TiO_2 -terminated surface indicates that the interfacial free energy of the Pd/ TiO_2 -STO interface is lower than that of the Pd/SrO-STO interface.

For the TiO_2 -STO surface, the 5c and 10c Pd samples have a SD of ~ 0.5 nm, which is narrower than the SD of 5c and 10c Pd on the SrO-STO surface, which is ~ 2 nm (Fig. 2). From the TEM images in Fig. 1, when the number of ALD cycles increase from 5c to 10c, Pd nanoparticles on the TiO_2 -terminated surface increase in average size, but the number of nanoparticles per unit area remains approximately constant. While Pd nanoparticles on the SrO-terminated surface increase in the number per area, the average size and size distribution are not substantially changed. This can be seen by comparing Fig. 1c and d to Fig. 1h and i. Note that the TEM image analysis of the Pd nanoparticles shown in Fig. 2 is unable to account for nanoparticles with diameters smaller than 1 nm. Schematic diagrams describing the morphology and evolution of Pd nanoparticles on the TiO_2 - and SrO-STO surfaces are shown in Fig. 2c and f.

3.2. Pd loading and effective Pd coverage

The ICP-AES and XRF determined atomic percentage ratios for Pd to Sr are listed in Table 1 along with the calculated Pd loading in wt.% and effective Pd coverages (detailed explanation in SM). As expected for ALD, the Pd wt.% loading exhibits approximately linear growth with the number of cycles. In order to normalize the loading of Pd on two different STO nanocuboids with different surface areas, we define 1 monolayer (ML) as the “effective Pd coverage (θ).” θ is equivalent to one Pd atom per Ti or Sr surface atom on an ideally terminated STO cube (6.56 nm^{-2}). Fig. 3 shows θ versus the number of ALD cycles. The higher θ on the TiO_2 -terminated surface implies that the interfacial free energy is more negative for Pd growth than on the SrO-terminated surface. This result is consistent with the fact that the Pd nanoparticle wets the TiO_2 -terminated surface better than the SrO-terminated surface. The argument above is consistent with the TEM images shown in Fig. 1.

3.3. Chemical state and structure analysis by XANES/EXAFS

The line shapes of the normalized XANES in Fig. 4a indicate that metallic Pd (Pd^0) and PdO (II) (Pd^{2+}) co-existed on both types of surface terminations. With the increasing number of ALD cycles, the Pd chemical state shifts monotonically from Pd^{2+} to Pd^0 .

The magnitudes of the Fourier transforms of the EXAFS spectra and the best fit to the first nearest neighbor coordination number (N) are shown in Fig. 4b. As listed in Table 2, the number of O nearest neighbors to Pd diminishes and the number of Pd neighbors increases as the number of ALD cycles increases. In ALD cycle 1c, only the Pd–O peak appears, indicating that the 1c sample behaves like PdO on both TiO_2 - and SrO-terminated surfaces. After subsequent ALD cycles, the Pd–Pd peak grows at the expense of the Pd–O peak, indicating the presence of more Pd in the metallic state (Pd^0). In addition, for the same number of ALD cycles, the fraction of palladium as Pd^0 is greater on the SrO-STO surface than on the TiO_2 -STO surface.

The EXAFS fitting result in Table 2 shows that for both of the terminations, the Pd–Pd coordination number ($N_{\text{Pd-Pd}}$) increases and the Pd–O coordination number ($N_{\text{Pd-O}}$) decreases as the number of ALD cycles increased. The σ , or the Debye–Waller factor (DWF), in the Pd nanoparticles is higher than the bulk value ($\sigma = 0.074 \text{ \AA}$ based on the Debye temperature of Pd, $\theta_{\text{D, Pd}} = 274 \text{ K}$). In general, the DWF increases as the size of the nanoparticle decreases because there is more surface, and at a surface the local DWF is always larger. However, the trend of

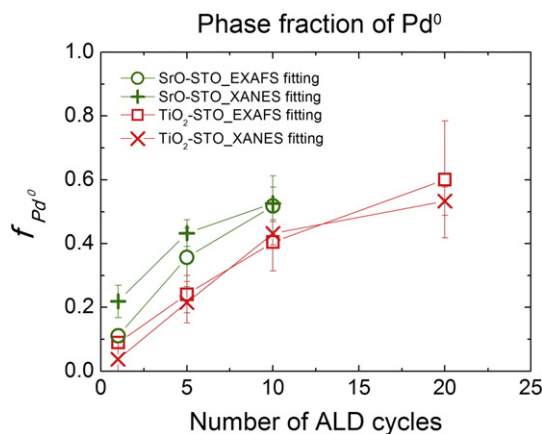


Fig. 5. Atomic phase fraction of Pd^0 (f_{Pd^0}) in Pd nanoparticles with the number of ALD cycles. f_{Pd^0} increases monotonically as the number of ALD cycles increases; and f_{Pd^0} is higher on the SrO-STO surface at the same number of ALD cycles.

DWF decreasing is not observable because of the relatively large uncertainties.

The atomic fraction of Pd in the Pd^0 and Pd^{2+} chemical states, namely f_{Pd^0} and $f_{\text{Pd}^{2+}} = 1 - f_{\text{Pd}^0}$, is calculated from both the linear combination fitting of XANES and the first shell coordination numbers (N) of Pd–Pd and Pd–O bonding fitted from the EXAFS (Details in SM). As seen in Fig. 5, the atomic fractions obtained from both XANES and EXAFS agree with each other. The atomic fraction of Pd^0 monotonically increases with the number of ALD cycles, and is greater on the SrO surfaces than on the TiO_2 surfaces.

3.4. In-situ EXAFS measurements of $N_{\text{Pd-Pd}}$ under reduction conditions

Although TEM is an effective tool for imaging the size of Pd nanoparticles directly, it is difficult to establish statistically significant measurements of the size of Pd nanoparticles when the loading is very low. It has been proposed that the coordination number of the first nearest neighbors (N) has a positive correlation with the size of the metallic nanoparticles [31,32]. Thus, EXAFS could serve as a good complementary characterization tool for measuring the size of nanoparticles. The in-situ EXAFS measurements were completed in H_2 flow at room temperature. Under this condition, hydrogen dissolves into interstitial sites in the Pd lattice and forms a Pd hydride, causing a slight expansion in the Pd lattice [33–36]. The expansion can be seen from the $R_{\text{Pd-Pd}}$ values

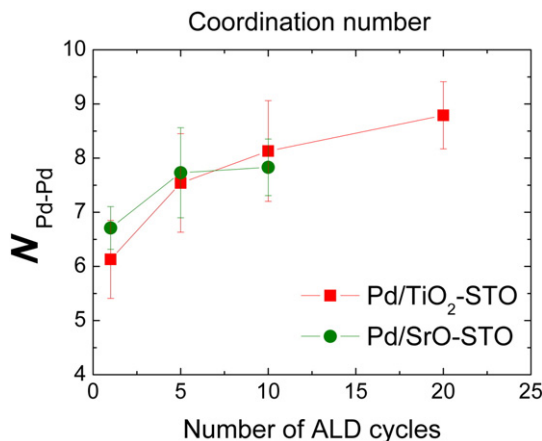


Fig. 6. First shell coordination number of Pd ($N_{\text{Pd-Pd}}$) extracted from the in-situ EXAFS measurement as a function of the number of ALD cycles. The measurements were performed after the residual Pd oxide on the Pd/STO samples was removed under flowing H_2 at $300 \text{ }^\circ\text{C}$ for 30 min.

listed in Table S3, which are 1 to 2% larger than that of the Pd foil. Despite this lattice expansion, the FCC structure of the Pd sublattice is retained [36,37]. Therefore N , which is related to the sublattice structure of Pd, is unchanged by Pd hydride formation. Thus N can still be applied as a probe reflecting the trend in Pd nanoparticle size evolution.

Fig. 6 shows that $N_{\text{Pd-Pd}}$ on the TiO_2 -terminated surface increases monotonically as the number of ALD cycles increases; whereas the same quantity on the SrO-terminated surface levels off after 5c. The result implies that the mean size of Pd nanoparticles on the TiO_2 -STO surface continued to increase over the range of 1–20 cycles. For the SrO-STO surface, the Pd nanoparticles grow in size from 1c to 5c, but stop increasing after 5c. This EXAFS result is consistent with the nanoparticle size trend seen by TEM in Fig. 1. For both surfaces, the Pd nanoparticle grows more significantly during the first ALD cycle than the subsequent cycles. The phenomena are similar to the result of ALD-Pt on the SrO-terminated nanocuboids reported in [38].

3.5. Mechanism of ALD-Pd nanoparticle growth on TiO_2 - and SrO-STO surfaces

Combining the data described in the above paragraphs, a model for the mechanism of ALD-Pd nanoparticle growth on the STO surfaces

can be proposed. The growth of Pd on TiO_2 -terminated STO surface is similar to the “nucleation and growth model” described in [38]. In this mechanism, single Pt atoms deposited on the surface are able to move across the surface and merge into the existing nuclei. However, the growth of Pd on the SrO-STO surface cannot be simply explained by the nucleation and growth model only. The residual ligands left on the STO surface from the Pd precursor, $\text{Pd}(\text{hfac})_2$, have to be taken into account as well. In previous ALD-Pd studies on both Al_2O_3 and TiO_2 supports, it was shown that $\text{Pd}(\text{hfac})_2$ dissociates into surface $(\text{hfac})^*$ species, which are incompletely removed by subsequent formalin cycles [39–41]. Meanwhile, the surface $(\text{hfac})^*$ species start to decompose creating surface F^* species when the temperature is above 100°C [41]. For our ALD growth temperature of 200°C , XPS on both TiO_2 - and SrO-terminated supports (Fig. 7a) show F 1s core level peaks with binding energies at 685 and 689 eV consistent with that of $-\text{F}$ and $-\text{CF}_3$ species, respectively as reported in [41–43]. The XPS result indicates the existence of residual $(\text{hfac})^*$ species on both the TiO_2 - and SrO-STO surfaces after ALD Pd growth.

The degree of interaction between the hfac species and the STO surface is likely responsible for the difference in Pd growth pattern. The hfac ligand is acidic and will interact more strongly with the basic SrO-STO surface than the neutral TiO_2 -STO surface [3,10]. In the XPS

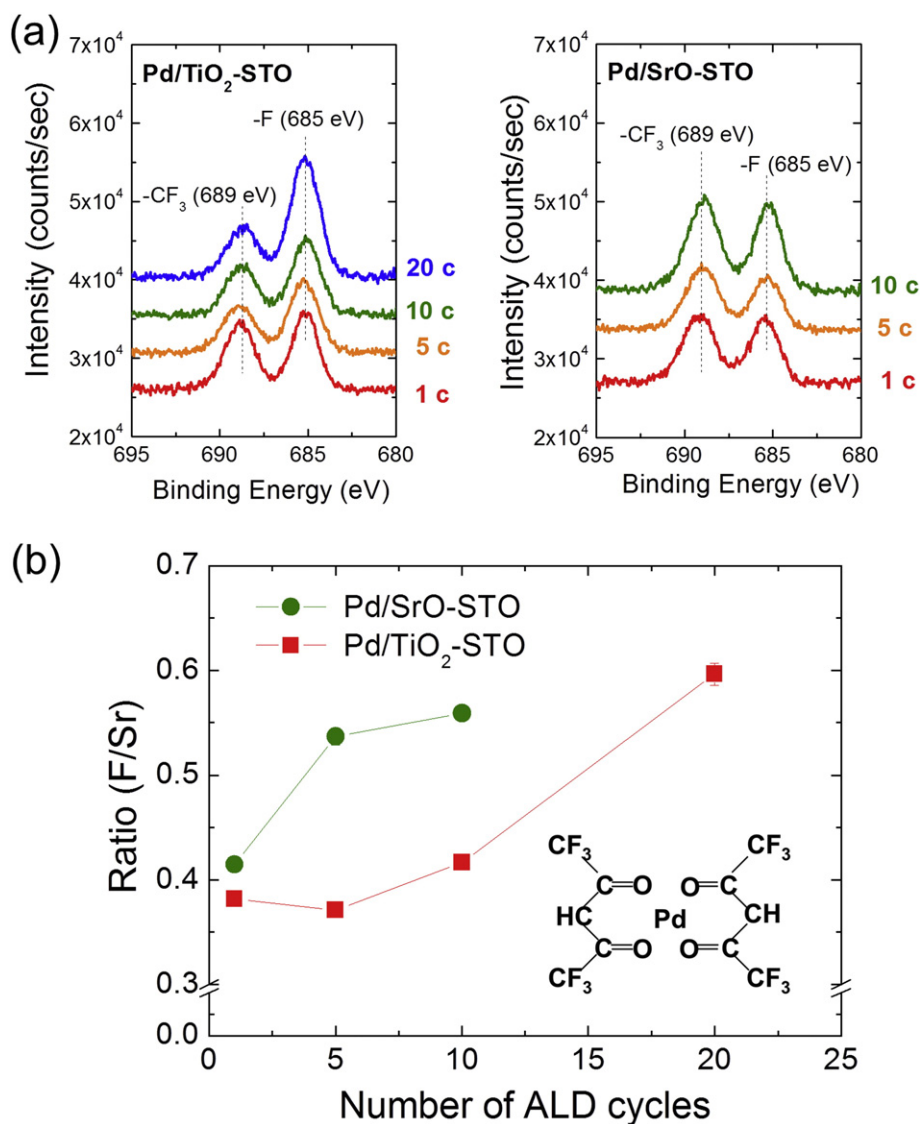


Fig. 7. (a) X-ray photoemission spectra of F 1s peaks of the Pd/ TiO_2 -STO and Pd/SrO-STO samples. (b) The atomic ratio between F and surface Sr atoms. The inserted image in 7b shows the structure of a $\text{Pd}(\text{hfac})_2$ molecule, which has 12 fluorine atoms.

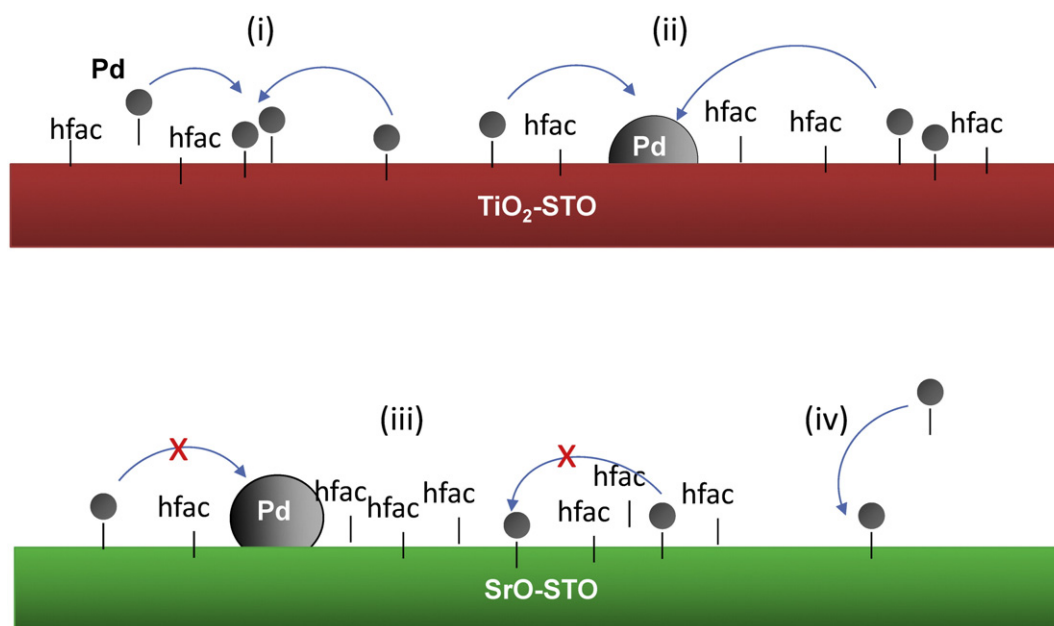


Fig. 8. Schematic representations of the growth of ALD Pd nanoparticles on the TiO_2 - and SrO -terminated STO surfaces. On the TiO_2 -STO surface, Pd follows the “nucleation and growth model,” in which Pd atoms are able to migrate across the surface to form nuclei because the hfac species on the surface weakly bounded (i). The nucleus grows from the migration of the Pd atoms in the subsequent ALD cycles (ii). On the SrO -STO surface, Pd follows the “trapped Pd model,” in which the migration of Pd is hindered by the strongly bonded hfac species (iii). In the subsequent ALD cycles, Pd forms secondary nuclei on hfac free area (iv).

analysis, the atomic ratios between F and Sr for the Pd/SrO-STO samples are higher than the Pd/ TiO_2 -STO samples (Fig. 7b, also see SM for details in calculation), indicating a higher coverage of hfac species remaining on the SrO-STO surface. The strongly bonded hfac species on the SrO surface hinders the migration of deposited Pd atoms across the surface to combine with existing nuclei, and leads to the formation of secondary nuclei in subsequent ALD cycles. Consequently, the Pd nanoparticle density for 10c is higher than that of 5c on the SrO-STO surface, as shown in the TEM images in Fig. 1. The formation of secondary nuclei also explains the wide size distribution of Pd nanoparticles on the SrO-STO surface. The increase in Pd nanoparticle size is inhibited by the number of hfac species surrounding the Pd nanoparticle. The nanoparticle can grow until the free Pd atoms within the migration distance are entirely consumed. The hfac species are expected to be statistically distributed over the SrO surface; therefore, the size of the Pd nanoparticle at a spot closer to more hfac species will be larger, and vice versa.

Furthermore, from the EXAFS fitting of $N_{\text{Pd-Pd}}$ (Fig. 6), the trapped Pd single atoms (or clusters) lower the average $N_{\text{Pd-Pd}}$ in the Pd nanoparticles on the SrO surface. This explains why TEM determined average size of Pd is larger on the SrO surface, but the $N_{\text{Pd-Pd}}$ value is not reflecting the TEM determined size: the trapped Pd is beyond the resolution of the TEM (<1 nm). On the other hand, the reason why the Pd on SrO 5c behaves more like Pd^{2+} than the SrO 10c can be rationalized as the following: on the surface of 5c, the smaller trapped Pd are easier to oxidize, which makes the 5c appears more oxidized. During the subsequent ALD cycles, secondary Pd nuclei sites start to grow and reduce the percentage of trapped Pd clusters. Therefore, the Pd in the SrO 10c sample appears more reduced than the 5c sample. A schematic representation of the “nucleation and growth model” and “trapped Pd model” can be found in Fig. 8.

3.6. In-situ XANES measurements of Pd/STO under redox environment

In order to track the oxidation state change of Pd under environmental conditions similar to a catalytic reaction, in-situ XANES was used to measure the oxidation state change of Pd at each step of a redox

reaction. Based on Fig. 3, the effective Pd coverages for the 5c/ TiO_2 -STO and 10c/SrO-STO are similar (approximately 0.8 ML). Therefore, the two samples were chosen for comparison of their behavior under redox conditions. The in-situ XANES redox measurements (Fig. 9) show that the oxidation state of Pd on both TiO_2 - and SrO-terminated surfaces can be shifted to either Pd^0 or Pd^{2+} state by exposing the Pd/STO sample to H_2 or O_2 gas at 300°C , and the transition is reversible. This indicates that both of the Pd/STO catalysts have the potential to sustain multiple oxidation/reduction cycles in catalytic reactions.

4. Summary and conclusion

The morphological and chemical properties of ALD-grown Pd nanoparticles supported on TiO_2 -STO and SrO-STO nanocuboids with well-

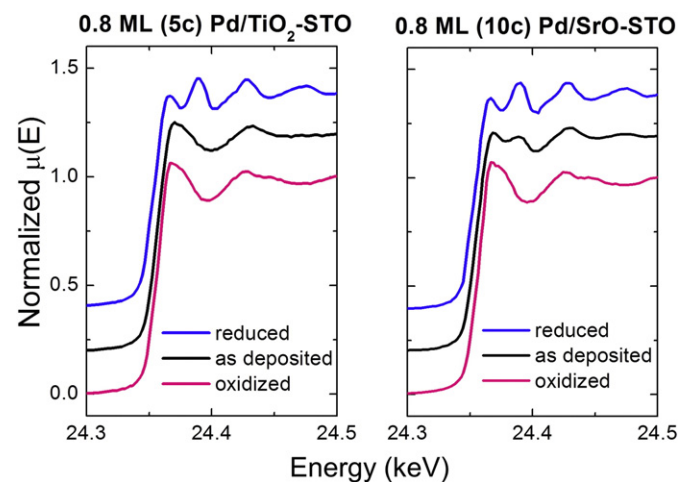


Fig. 9. Pd K-edge in-situ XAFS measurements of 0.8 ML Pd on the TiO_2 - and SrO-terminated STO surfaces. The measurements were performed at 300°C under H_2/O_2 redox conditions and were shown to be reversible.

defined (001) surface are characterized and compared by the combined analysis of TEM, XRF, XANES, EXAFS, and XPS. The Pd nanoparticle exhibits better wetting on the TiO₂–STO surface than on the SrO–STO surface, indicating lower interfacial free energy between Pd/TiO₂–STO than Pd/SrO–STO interface. The contrasting wetting property may offer opportunities for controlling the morphology and exposed facets of Pd nanoparticles by different surface terminations of the support oxide. In addition, the number of the ALD cycles is able to control the effective Pd coverage and the fraction of Pd⁰. The coverage and Pd⁰ fraction are found to increase monotonically with the number of ALD cycles on both supports.

As the loading of Pd increases, the Pd nanoparticles grow in number on the SrO–STO surface, but in size on the TiO₂–STO surface. The difference in the growth behavior is attributed to the interaction between the STO surface and the residual hfac species from the Pd precursor. The strongly-bounded hfac species hinder the migration of Pd atoms on the SrO–STO surface and leave single Pd atoms or sub-critical nuclei trapped. Thus, the Pd nanoparticles grow by forming secondary nuclei on the SrO–STO surface. Different from the SrO–STO surface, the Pd nanoparticles on the TiO₂–STO surface are not affected by the relatively weakly-bounded hfac species. Therefore, the Pd nanoparticles follow a nucleation and growth mechanism and grow in size.

The result has demonstrated the feasibility of applying the Pd/STO metal/support oxide system to investigate the relationship between the structure of metal catalysts and the performance. We expect that this approach can be further employed for other metal/support oxide systems.

Acknowledgments

This work was supported by the Institute for Catalysis in Energy Processes (ICEP) at Northwestern University (NU) under DOE Grant DE-FG02-03ER15457. Electron microscopy was performed at the EPIC facility support by the NU-MRSEC program (NSF DMR-1121262). X-ray measurements were performed at the Advanced Photon Source of Argonne National Lab (ANL), at DND-CAT (Sector 5), which is supported by E.I. DuPont de Nemours & Co., NU and The Dow Chemical Co. ANL is supported by DOE under grant number DE-AC02-06CH11357. The X-ray photoemission work was performed in the Keck-II facility of the NUANCE Center at NU. BRC is partially supported by Study Abroad Fellowship from Ministry of Education of Taiwan. LC is supported by a National Science Foundation Graduate Research Fellowship. We thank Qing Ma at DND-CAT for assisting with the XAFS measurements.

Appendix A. Supplementary data

Supplementary data to this article can be found online at <http://dx.doi.org/10.1016/j.susc.2015.10.057>.

References

- [1] W.L. Winterbottom, *Acta Metall.* 15 (1967) 303.
- [2] F.A. Rabuffetti, H.S. Kim, J.A. Enterkin, Y.M. Wang, C.H. Lanier, L.D. Marks, K.R. Poeppelmeier, P.C. Stair, *Chem. Mater.* 20 (2008) 5628.
- [3] F.A. Rabuffetti, P.C. Stair, K.R. Poeppelmeier, *J. Phys. Chem. C* 114 (2010) 11056.
- [4] L.H. Hu, C.D. Wang, S. Lee, R.E. Winans, L.D. Marks, K.R. Poeppelmeier, *Chem. Mater.* 25 (2013) 378.
- [5] L. Crosby, J. Enterkin, F. Rabuffetti, K. Poeppelmeier, L. Marks, *Surf. Sci.* 632 (2015) L22.
- [6] S.T. Christensen, et al., *Small* 5 (2009) 750.
- [7] J.A. Enterkin, W. Setthapun, J.W. Elam, S.T. Christensen, F.A. Rabuffetti, L.D. Marks, P.C. Stair, K.R. Poeppelmeier, C.L. Marshall, *ACS Catal.* 1 (2011) 629.
- [8] J.A. Enterkin, K.R. Poeppelmeier, L.D. Marks, *Nano Lett.* 11 (2011) 3510.
- [9] J.A. Enterkin, R.M. Kennedy, J.L. Lu, J.W. Elam, R.E. Cook, L.D. Marks, P.C. Stair, C.L. Marshall, K.R. Poeppelmeier, *Top. Catal.* 56 (2013) 1829.
- [10] Y.Y. Lin, J.G. Wen, L.H. Hu, R.M. Kennedy, P.C. Stair, K.R. Poeppelmeier, L.D. Marks, *Phys. Rev. Lett.* 111 (2013) 156101.
- [11] A.D. Polli, T. Wagner, T. Gemming, M. Rühle, *Surf. Sci.* 448 (2000) 279.
- [12] F. Silly, A.C. Powell, M.G. Martin, M.R. Castell, *Phys. Rev. B* 72 (2005) 165403.
- [13] F. Silly, M.R. Castell, *J. Phys. Chem. B* 109 (2005) 12316.
- [14] H. Iddir, V. Komanicky, S. Ogut, H. You, P. Zapol, *J. Phys. Chem. C* 111 (2007) 14782.
- [15] V. Komanicky, H. Iddir, K.C. Chang, A. Menzel, G. Karapetrov, D.C. Hennessy, P. Zapol, H. You, *Electrochim. Acta* 55 (2010) 7934.
- [16] S.T. Christensen, J.W. Elam, B. Lee, Z. Feng, M.J. Bedzyk, M.C. Hersam, *Chem. Mater.* 21 (2009) 516.
- [17] S.T. Christensen, B. Lee, Z.X. Feng, M.C. Hersam, M.J. Bedzyk, *Appl. Surf. Sci.* 256 (2009) 423.
- [18] Z.X. Feng, S.T. Christensen, J.W. Elam, B. Lee, M.C. Hersam, M.J. Bedzyk, *J. Appl. Phys.* 110 (2011).
- [19] R.G. Carr, G.A. Somorjai, *Nature* 290 (1981) 576.
- [20] S.E. Stoltz, D.E. Ellis, M.J. Bedzyk, *Surf. Sci.* 630 (2014) 46.
- [21] S.E. Stoltz, D.E. Ellis, M.J. Bedzyk, *Surf. Sci.* 633 (2015) 8.
- [22] Z.X. Feng, A. Kazimirov, M.J. Bedzyk, *ACS Nano* 5 (2011) 9755.
- [23] J.W. Elam, A. Zinovev, C.Y. Han, H.H. Wang, U. Welp, J.N. Hryn, M.J. Pellin, *Thin Solid Films* 515 (2006) 1664.
- [24] S.T. Christensen, H. Feng, J.L. Libera, N. Guo, J.T. Miller, P.C. Stair, J.W. Elam, *Nano Lett.* 10 (2010) 3047.
- [25] H. Feng, J.W. Elam, J.A. Libera, W. Setthapun, P.C. Stair, *Chem. Mater.* 22 (2010) 3133.
- [26] H. Feng, J.A. Libera, P.C. Stair, J.T. Miller, J.W. Elam, *ACS Catal.* 1 (2011) 665.
- [27] J.W. Elam, M.D. Groner, S.M. George, *Rev. Sci. Instrum.* 73 (2002) 2981.
- [28] C.A. Schneider, W.S. Rasband, K.W. Eliceiri, *Nat. Methods* 9 (2012) 671.
- [29] B. Ravel, M. Newville, *J. Synchrotron Radiat.* 12 (2005) 537.
- [30] P.J. Chupas, K.W. Chapman, C. Kurtz, J.C. Hanson, P.L. Lee, C.P. Grey, *J. Appl. Crystallogr.* 41 (2008) 822.
- [31] A. Frenkel, *Z. Kristallogr.* 222 (2007) 605.
- [32] A.I. Frenkel, C.W. Hills, R.G. Nuzzo, *J. Phys. Chem. B* 105 (2001) 12689.
- [33] J.A. Mccauley, *J. Phys. Chem.* 97 (1993) 10372.
- [34] M.W. Tew, J.T. Miller, J.A. van Bokhoven, *J. Phys. Chem. C* 113 (2009) 15140.
- [35] M.W. Tew, M. Janousch, T. Huthwelker, J.A. van Bokhoven, *J. Catal.* 283 (2011) 45.
- [36] J.Q. Wang, Q. Wang, X.H. Jiang, Z.N. Liu, W.M. Yang, A.I. Frenkel, *J. Phys. Chem. C* 119 (2015) 854.
- [37] F.A. Lewis, *Platin. Met. Rev.* 4 (1960) 132.
- [38] C. Wang, L. Hu, K. Poeppelmeier, P.C. Stair, L. Marks, *J. Phys. Chem.* (2015) submitted for publication.
- [39] D.N. Goldstein, S.M. George, *Thin Solid Films* 519 (2011) 5339.
- [40] Y. Lei, et al., *J. Phys. Chem. C* 117 (2013) 11141.
- [41] A. Gharachorlou, M.D. Detwiler, A.V. Nartova, Y. Lei, J.L. Lu, J.W. Elam, W.N. Delgass, F.H. Ribeiro, D.Y. Zemlyanov, *ACS Appl. Mater. Interfaces* 6 (2014) 14702.
- [42] W.B. Lin, B.C. Wiegand, R.G. Nuzzo, G.S. Girolami, *J. Am. Chem. Soc.* 118 (1996) 5977.
- [43] S.G. Rosenberg, M. Barclay, D.H. Fairbrother, *ACS Appl. Mater. Interfaces* 6 (2014) 8590.